Emergent entanglement phase transitions in non-Hermitian Aubry-André-Harper chains

Shan-Zhong Li,[1,2,3] Xue-Jia Yu,[1,4,*] and Zhi Li[2,3,†]

[1]*Department of Physics, Fuzhou University, Fuzhou 350116, Fujian, China*

[2]*Key Laboratory of Atomic and Subatomic Structure and Quantum Control (Ministry of Education), Guangdong Basic Research Center of Excellence for Structure and Fundamental Interactions of Matter, School of Physics, South China Normal University, Guangzhou 510006, China*

[3]*Guangdong Provincial Key Laboratory of Quantum Engineering and Quantum Materials, Guangdong-Hong Kong Joint Laboratory of Quantum Matter, Frontier Research Institute for Physics, South China Normal University, Guangzhou 510006, China*

[4]*Fujian Key Laboratory of Quantum Information and Quantum Optics, College of Physics and Information Engineering, Fuzhou University, Fuzhou, Fujian 350108, China*

(Received 8 September 2023; revised 26 November 2023; accepted 5 January 2024; published 16 January 2024)

We investigate the entanglement dynamics of the non-Hermitian Aubry-André-Harper chain. The results reveal that by increasing quasiperiodic strength, a phase transition occurs from the area law induced by non-Hermitian skin effect to the area law arising from Anderson localization. For the former, the entanglement entropy follows a nonmonotonic process, i.e., it increases first, then oscillates, and finally converges to a stable value while, for the latter, the entanglement entropy remains low because the wave function is not expandable in Anderson's localization region. The early-stage behavior of entanglement entropy indicates that the two area-law cases are of different phases. Interestingly, the volume-law behavior emerges at the critical point between these two area-law phases. Our study reveals that the area laws induced by the skin effect and the Anderson localization are two different phases, and that a volume law can emerge at the phase transition point. The understanding of the entanglement phase transition induced by disorder and skin effect is thus deepened.

DOI: 10.1103/PhysRevB.109.024306

I. INTRODUCTION

Rapid development of experimental platforms for quantum simulations drives exploration of nonequilibrium dynamics [1–6]. In recent years, significant attention has been directed towards non-Hermitian Hamiltonians [7–51], as they effectively describe the physical characteristics of open and nonconservative systems. One of the unique phenomena is the famous non-Hermitian skin effect, and this asymmetric hoppings-induced effect can make the spectrum and eigenstates very much sensitive to boundary conditions [26]. The skin effect holds a pivotal position in the realm of non-Hermitian topological band theories [26–39]. Under open boundary conditions (OBCs), eigenstates become exponentially localized at the system's boundaries, disrupting the conventional bulk-boundary correspondence. Consequently, non-Hermitian bulk-boundary correspondence [28,33] and the non-Bloch band theory [26,31] are invoked to account for the unconventional behavior induced by the skin effect. In the context of OBCs, the skin effect confines the macroscopic particle flow to the boundaries [40], restraining the growth of entanglement entropy and adhering to the area law [52].

In addition, Anderson localization also contributes to the suppression of entanglement entropy growth [42,44,53,54]. When disorder or quasiperiodic exceeds a threshold, the system undergoes a transition from an extended phase to a localized phase [55–59]. Although both skin effect and Anderson localization can induce localized states, their eigenstate characteristics are completely different, i.e., the former is localized on the boundary, while the latter is localized in the bulk of the system. In low-dimensional ($d \leqslant 2$) systems, even minor disorder can drive the system into a localized phase, rendering the extended-localized transition absent in such cases [60]. In the three-dimensional case, weak disorder can lead to the coexistence of extended and localized states, which is clearly divided by the critical energy mobility edge [57,61]. In other words, under such circumstances, one can achieve the metal-insulator phase transition by manipulating the Fermi surface.

Replacing random disorder with a quasiperiodic potential has been demonstrated to induce a metal-insulator transition [56] and mobility edge [62–73] in low-dimensional systems. The one-dimensional Aubry-André-Harper (AAH) model is one of the most notable quasiperiodic examples [56,74]. When one introduces asymmetric hopping to the AAH model, the extended phase gradually transforms into a skin-localized phase under OBCs. The increase of quasiperiodic intensity weakens the skin effect, and the phase transition from the skin state to the Anderson localized state occurs gradually [41]. The related dynamics have been extensively studied [44,75–80]. In addition, the change of entanglement entropy is accompanied by the phase transition from the skin phase to the localized phase. Then how does the entanglement behavior

*xuejiayu@fzu.edu.cn
†lizphys@m.scnu.edu.cn

change before and after the phase transition? Does it vary depending on the boundary conditions one chooses? What are the characteristics of the critical points between them?

To address the above questions, we investigate the entanglement dynamics of the AAH model with asymmetric (nonreciprocal) hopping. Under OBCs, Anderson localization is accompanied by a reentrant area law ($S \propto L^{d-1}$) in entanglement entropy, i.e., transitioning from an area law induced by the skin effect to another area law induced by Anderson localization. The two area laws induced by these two different mechanisms can be distinguished by the early stages entanglement dynamics. Entanglement entropy under the skin effect exhibits initial growth, followed by a period of oscillation, and then gradual reduction. The nonmonotonic growth observed in the early stages of evolution, as revealed through the density distribution, is driven by the skin effect, which forces particles to move along a unidirection. We demonstrate through an early stage of entanglement dynamics and density evolution with different initial states that the time it takes for particles to accumulate at the boundary corresponds to the time it takes for entanglement entropy to decrease to a stable value. In contrast, under Anderson localization, the particles are localized at the initial position, which makes the entanglement entropy hardly grow. This early behavior is clearly illustrated by two different area law phases. Interestingly, by observing the scaling behavior at a critical line, we find that a volume law ($S \propto L^d$) can emerge between the two different types of area-law regions. Furthermore, we also discuss the entanglement phase transition under periodic boundary conditions (PBCs). As the quasiperiodic strength increases, a log-area law entanglement phase transition occurs, which again satisfies the volume law at its critical point.

The organization of this paper is as follows. In Sec. II, we introduce the model and outline the method for calculating the entanglement entropy. In Sec. III, we use the evolution of the early entanglement entropy and density distributions to distinguish between two different area-law regions. In Sec. IV, we investigate the scaling behavior of the critical point between two area-law regions in the non-Hermitian AAH model. In Sec. V, we discuss the case of PBCs. In Sec. VI, we presents a summary of the entire work. In Appendix A, we give more details on computing entanglement entropy. In Appendix B, We discuss the localization phase transition of the system and the multifractal properties on the critical line. In Appendix C, We give the variation of entanglement entropy with system size for small asymmetric hopping strengths.

II. MODEL AND ENTANGLEMENT ENTROPY

We consider a non-Hermitian AAH model with asymmetric hopping and the Hamiltonian can be defined as

$$H = \sum_{j=1}^{L-1}(J_L c_j^\dagger c_{j+1} + J_R c_{j+1}^\dagger c_j) + \sum_{j=1}^{L} 2\lambda\cos(2\pi\alpha j + \theta)c_j^\dagger c_j, \tag{1}$$

where c_j ($c_j^\dagger$) is the fermionic annihilation (creation) operator at the jth site and L is the total number of the lattice. $J_L = -(J-\gamma)/2$ and $J_R = -(J+\gamma)/2$, with J and γ being real parameters depicting the strengths of symmetric and asymmetric hopping, respectively. The on-site potential strength is governed by the quasiperiodic strength λ. α is the quasiperiodic parameter and θ is a random phase. When $\gamma = 0$, $\lambda \neq 0$, Eq. (1) corresponds to the AAH model, with a localization transition point at $\lambda = 0.5$ [56]. When $\lambda = 0$, $\gamma \neq 0$, Eq. (1) reduces to the Hatano-Neslon model [81], which has skin effects under OBCs and has been extensively studied in the field of non-Hermitian topological insulator [26–39]. This asymmetric hopping can be realized by the quantum trajectory approach [28,40]. When $\gamma \neq 0$ and $\lambda \neq 0$, the localization transition point is given by $\lambda = \max\{|J_R|, |J_L|\}$ [41]. All eigenstates at the OBC (PBC) before reaching the critical quasiperiodic strength are skin states (extended states), and beyond the critical strength, they become Anderson localized states. Details about Anderson localization can be found in Appendix B. In the following, we will set $J = 1$ as the units of energy, $\alpha = (\sqrt{5}-1)/2$, $\lambda > 0$ and $\gamma < 0$.

To study the dynamical behavior of entanglement entropy, we choose the Neél state $|\psi_0\rangle = \prod_{j=1}^{L/2} c_{2j}^\dagger |\text{vac}\rangle$ as the initial state, where $|\text{vac}\rangle$ is the fermionic vacuum state. The initial wave function evolves according to the non-Hermitian Hamiltonian H as

$$|\psi(t)\rangle = \frac{e^{-iHt}|\psi_0\rangle}{\|e^{-iHt}|\psi_0\rangle\|}. \tag{2}$$

Since the Hamiltonian in Eq. (1) is quadratic and the initial state $|\psi_0\rangle$ is a Slater determinant state, the final state $|\psi(t)\rangle$ is also a determinant state and its correlation matrix $C_{ij}(t) = \langle\psi(t)|c_i^\dagger c_j|\psi(t)\rangle$ can be efficiently calculated. The von Neumann entanglement entropy S between a subsystem $[x_1, x_2]$ and the rest of the system by [82]

$$S = -\sum_{i=1}^{x_2-x_1+1}[V_i\ln(V_i) + (1-V_i)\ln(1-V_i)], \tag{3}$$

where V_i is the ith eigenvalue of the correlation matrix C. In the next calculations, we consider only half-chain entanglement entropy, i.e., $x_1 = 1$ and $x_2 = L/2$, and denote this as $S_{L/2}$ (more details can be found in Appendix A). We note that in the numerical calculations, all quantities are averaged over 300 random quasiperiodic phases θ.

III. EARLY STATE ENTANGLEMENT DYNAMICS

In this section, we discuss the entanglement phase transitions for non-Hermitian AAH models under OBCs. The half-chain entanglement entropy $S_{L/2}$ of the steady state in the $\lambda - \gamma$ plane is shown in Fig. 1(a), where the black dashed line is the Anderson localization transition line $\lambda = (J-\gamma)/2$ [41]. In the case of $\gamma = 0$, as λ crosses the critical value of 0.5, the system undergoes an entanglement transition from a volume law to an area law due to the influence of Anderson localization, with the critical point exhibiting a volume law [54]. Clearly, the growth of entanglement entropy on both sides of the critical line is suppressed for $\gamma < 0$, but this is attributed to different mechanisms. On the left side of the critical line, when $\gamma \neq 0$, the skin effect propels particles towards the boundary, ultimately leading to particle localization at the boundary, reducing quantum jumps, and thus inhibiting the

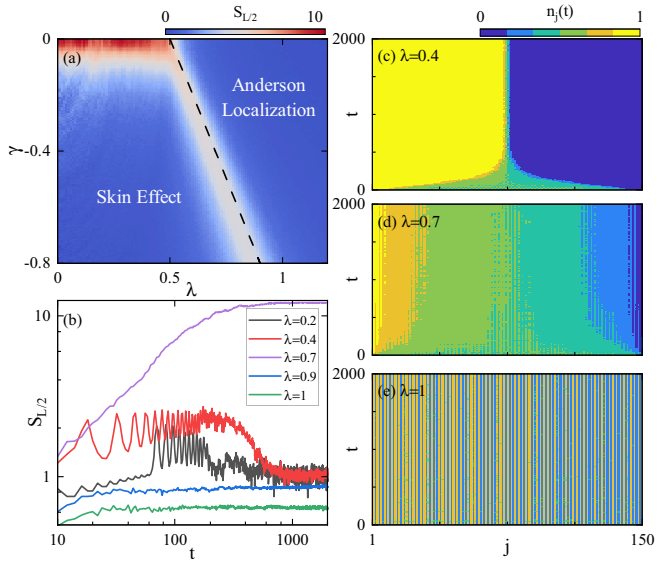

FIG. 1. (a) Steady-state half-chain entanglement entropy $S_{L/2}$ on the $\lambda - \gamma$ plane with the system size $L = 50$, where the black dashed line is $\lambda = (J - \gamma)/2$. (b) Time evolution of entanglement entropy $S_{L/2}$ for different λ. Time evolution of the density distribution $n_j(t)$ for (c) $\lambda = 0.4$, (d) $\lambda = 0.7$, and (e) $\lambda = 1$. For plots (b)–(e), $\gamma = -0.4$ and $L = 150$.

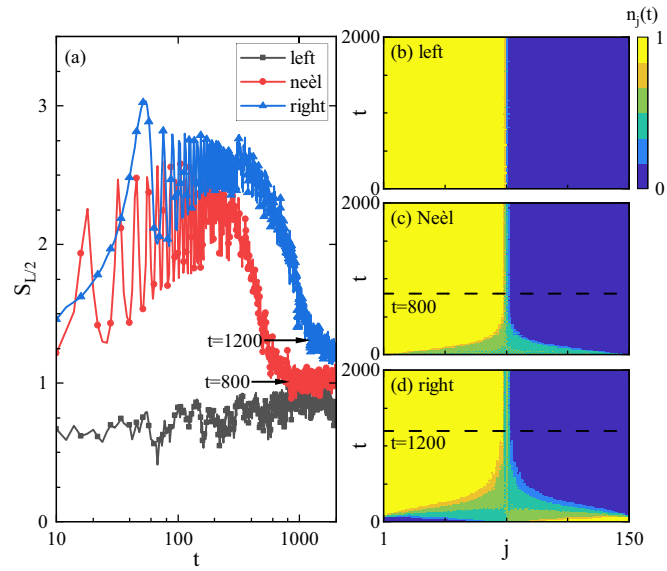

FIG. 2. (a) Time evolution of entanglement entropy $S_{L/2}$ for different initial states. Time evolution of the density distribution $n_j(t)$ in the initial state (b) left, (c) Neél, and (d) right. For all plots, $\gamma = -0.4$, $\lambda = 0.4$, and $L = 150$.

growth of entanglement entropy [40]. At the same time, we note that when $\gamma \to 0$, the system can obtain larger entanglement entropy (compared to the region with $\gamma < -0.3$), and we show that it remains an area law with further discussion in Appendix C. On the right side, Anderson localization results in exponential particle localization at the initial positions, suppressing the growth of entanglement entropy [42,44,53,54]. Both mechanisms suppress entanglement entropy, causing the system to follow the area law [40,42,44,53,54].

In fact, the area-law regions induced by these two different mechanisms can be distinguished by their early stage entanglement dynamics. In Fig. 1(b), we show the evolution of the early stage entanglement entropy $S_{L/2}$ for different λ with $\gamma = -0.4$. For $\lambda < 0.7$, the entanglement entropy initially increases, undergoes oscillations for a period, and then gradually decreases. This nonmonotonic time evolution of entanglement entropy has been reported in many studies [40,43,44,75,80,83]. For $\lambda > 0.7$, it consistently maintains a lower entanglement entropy. At the critical point $\lambda = 0.7$, the entanglement entropy monotonically increases and then reaches a large saturation value. The distinction between these two area laws can also be characterized through the evolution of the density distribution n_j, defined as

$$n_j(t) = \langle \psi(t) | c_j^\dagger c_j | \psi(t) \rangle. \tag{4}$$

The evolution of the particle density distribution for $\lambda = 0.4$, $\lambda = 0.7$, and $\lambda = 1$ with system size $L = 150$ is shown in Figs. 1(c)–1(e). For $\lambda = 0.4$, the skin effect pushes the particles in the direction imposed by the asymmetry, leading to an increase in early stage entanglement entropy. This phenomenon continues until the particles gradually localize at the boundary, before decreasing to a stable value. When $\lambda = 1$, Anderson localization restricts particle transport, resulting in no increase in the entanglement entropy during both short- and long-time evolution, always maintaining the information from the initial moment. For the critical point $\lambda = 0.7$, the long-time propagation of particles causes the entanglement entropy to grow.

In addition, the density evolution and the entanglement entropy reach a stable value at the same time. We consider other two initial states, localized in the left- and right-half chains, defined, respectively, as

$$\begin{aligned} |\text{left}\rangle &= \textstyle\prod_{j=1}^{L/2} c_j^\dagger |\text{vac}\rangle, \\ |\text{right}\rangle &= \textstyle\prod_{j=1}^{L/2} c_{L/2+j}^\dagger |\text{vac}\rangle, \end{aligned} \tag{5}$$

and U_0 corresponding to these two states are $[U_0]_{jk} = \delta_{j,k}$ and $[U_0]_{jk} = \delta_{L/2+j,k}$, respectively (for details, see Appendix A). Together with the Neél state, the time evolution of the density distribution $n_j(t)$ for the three different initial states at $\lambda = 0.4$ is shown in Fig. 2(a). For the left state (localized in the left half chain), the entanglement entropy behaves similarly to that of the Anderson localized, maintaining relatively low values throughout. However, for the Neél state and the right state (localized in the right-half chain), the entanglement entropy exhibits an initial increase, followed by oscillations, and eventually decreases. We have provided approximate times required for the initial Neél state and right state to reach a steady state in the figures, which are $t = 800$ and $t = 1200$, respectively. By comparing this with the density distribution in Figs. 2(b)–2(d), one can see that the initial position of the left state lies on the skin boundary, so the particle does not diffuse and therefore the entanglement entropy does not increase, exhibiting a behavior similar to that of Anderson localization. Conversely, for the initial Neél and right states, the skin effect drives particle propagation towards the skin boundary, and the localization is at the boundary for the same time as the entanglement entropy reaches a stable value.

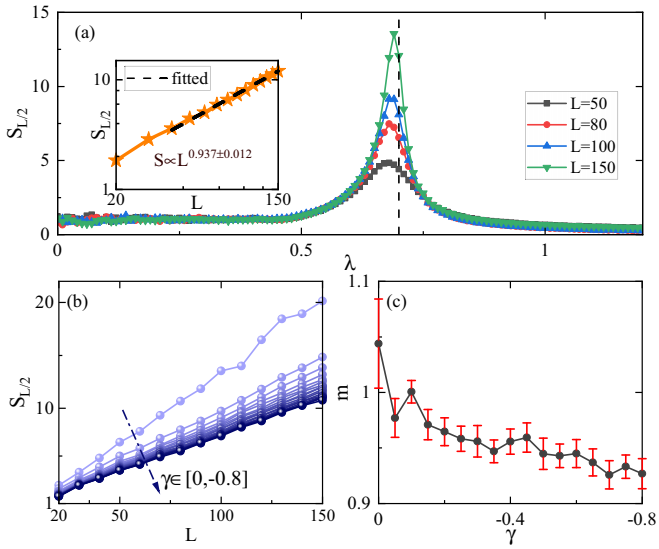

FIG. 3. (a) Entanglement entropy $S_{L/2}$ as a function of λ for different L with $\gamma = -0.4$. The inset shows the data for $\lambda = 0.7$ in a log-log scale with a power-law fit described by $S_{L/2} \propto L^{0.937\pm0.012}$ and the black dashed line represents the transition point between the two area-law regions with $\lambda = 0.7$. (b) Entanglement entropy as a function of L for different γ, where the darker the color the smaller the γ, and $\lambda = (J - \gamma)/2$. (c) The exponent m fitted as a function of γ in the form $S \propto L^m$.

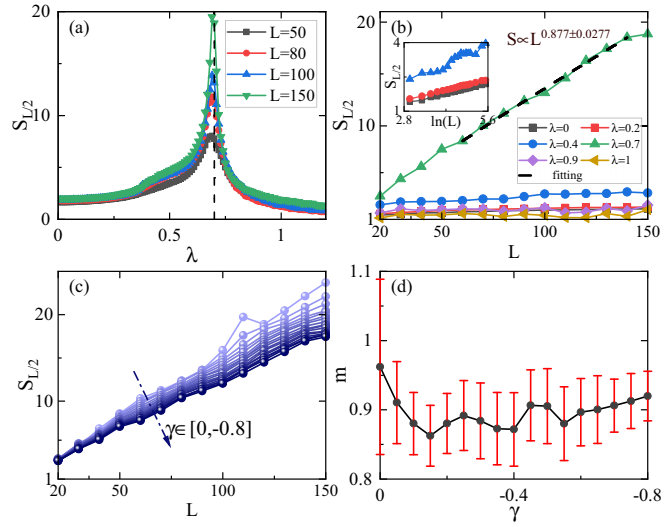

FIG. 4. (a) Entanglement entropy $S_{L/2}$ as a function of λ for different L with $\gamma = -0.4$, where the black dashed line represents the transition point between the two area-law regions with $\lambda = 0.7$. (b) The linear-log plot of the entanglement entropy $S_{L/2}$ as a function of L for different λ. The inset shows $S_{L/2}$ in log-linear coordinates for $\lambda = 0, 0.2, 0.4$ with L up to 250. (c) Entanglement entropy as a function of L for different γ, where the darker, the color the smaller the γ, and $\lambda = (J - \gamma)/2$. (d) The fitting exponent m as a function of γ.

IV. ENTANGLEMENT PHASE TRANSITION

The early entanglement dynamics provide a clear distinction between these two area-law regions, indicating different phases. Naturally, an interesting question arises: Is there an entangled phase transition between two different area-law regions? Do the phase transition points still follow the area law? The time evolution of entanglement entropy at the critical point $\lambda = 0.7$ can reach a relatively large saturation value, which suggests that a new law emerges at the critical point. In Fig. 3(a), we present the entanglement entropy $S_{L/2}$ as a function of λ for various system sizes L with $\gamma = -0.4$. It can be observed that at the critical point $\lambda = J_L = 0.7$, the entanglement entropy increases with the enlargement of the system size, while the two regions governed by the area laws remain constant. In the inset, we fit the scaling behavior of the entanglement entropy at the critical point, which satisfies the nearly volume law $S_{L/2} \propto L^{0.937\pm0.012}$. That is, similar to the Hermitian case, the volume law on the critical point is robust even in the presence of the skin effect, which stems from the fact that the critical point remains a multifractal phase under the influence of asymmetry hopping, as discussed in Appendix B. Further, to verify whether the volume law is maintained at the critical line, we show the entanglement entropy as a function of L for γ from 0 to −0.8 in Fig. 3(b), where the darker the color the smaller the γ, and $\lambda = (J - \gamma)/2$. It is clear that the introduction of asymmetry hopping suppresses the steady-state entanglement entropy. However, in Fig. 3(c), where we used a power law form $S_{L/2} \propto L^m$ to fit the scaling of entanglement entropy, one can observe that $m > 0.9$ almost follows the volume law. This implies that the scaling behavior at the critical line is robust with respect to asymmetric hopping, and the volume law can emerge between the two area-law regions, leading to an area-area entanglement phase transition.

V. PERIODIC BOUNDARY CONDITIONS

In this section, we discuss the case of PBCs. In Fig. 4(a), we show the entanglement entropy $S_{L/2}$ as a function of λ for different system sizes L. In the absence of quasiperiodic potential, it has been demonstrated in Refs. [40,42] that the entanglement entropy satisfies the logarithmic relation $S_{L/2} = \frac{1}{3} \ln L$ with system size L. When $\lambda < 0.7$, the entanglement entropy still satisfies the logarithmic law [see inset of Fig. 4(b)]. For $\lambda > 0.7$, the Anderson localization makes the entanglement entropy follow the area law. However, at the critical point $\lambda = 0.7$, the entanglement entropy increases as the system size increases, forming a distinct peak. In Fig. 4(b), we show the entanglement entropy as a function of L for different λ. We fit m on the critical point by $S \propto L^m$ and $m = 0.877 \pm 0.027$ still almost keeps the volume law. Furthermore, in Fig. 4(c), we present the entanglement entropy $S_{L/2}$ as a function of L for critical line (the darker the color, the smaller the γ), and the fitted values of m are shown in Fig. 4(d). It can be observed that the introduction of asymmetric hopping γ slightly suppresses the growth of entanglement but almost maintains the volume law. Under PBCs, the increase of the quasiperiodic strength induces an entanglement phase transition of the log-area law, which is the same conclusion as in Ref. [44].

VI. CONCLUSION

In this paper, we focus on the entanglement dynamics of a non-Hermitian AAH chain with asymmetric hopping. We obtain the corresponding phase diagram for OBCs and PBCs, respectively.

On the one hand, for OBCs, the entanglement entropy of the system is suppressed both before and after the phase transition, showing the characteristics of area-law behavior. By further analyzing the entanglement dynamics and density distribution features in the early stage of evolution, we find that the system of the above two area laws belongs to different phases, which can be distinguished by the entanglement entropy. The difference between the two area-law phases means that a phase transition occurs between them. Note that, through finite-size scaling analysis, we find that the critical boundary of the phase transition exhibits the characteristics of volume law.

On the other hand, for PBCs, the disappearance of skin effect will cause logarithmic law behavior before the localization phase transition, thus giving rise to log-area law entanglement phase transition in the system. Furthermore, a similar critical boundary with volume law characteristics can emerge.

This paper reveals that the area-law phases induced by disorder and non-Hermitian are essentially different phases, and the phase transition points between them show the characteristics of volume law. This opens another avenue to explore entanglement phase transitions in non-Hermitian quasi-periodic disorder systems.

Note added. Recently, we became aware of Ref. [84], which similarly investigated entanglement phase transitions in non-Hermitian AAH models and revealed two entanglement phase transitions in non-Hermitian quasicrystals: the volume-area law and the log-area law. Here, in our paper, we discovered area-area law entanglement phase transitions under asymmetric hopping and that a volume law can emerge between two different area law phases. Note that the log-area law phase transition mentioned in Ref. [84] is a special case of our model under PBCs.

ACKNOWLEDGMENTS

We thank S.-L. Zhu, Y.-G. Liu, and E. Cheng for helpful discussions and constructive suggestions. This work was supported by the Guangdong Basic and Applied Basic Research Foundation (Grant No. 2021A1515012350) and the National Key Research and Development Program of China (Grant No. 2022YFA1405300). X.-J.Y. acknowledges support from start-up Grant No. XRC-23102 of Fuzhou University.

APPENDIX A: DETAILS OF THE CALCULATION OF ENTANGLEMENT ENTROPY

Here, we will give the details of computing the entanglement entropy (also see Refs. [40,42]). The dynamics of the initial neél state $|\psi_0\rangle = \prod_{j=1}^{L/2} c_{2j}^\dagger |\text{vac}\rangle$ at the free fermions Hamiltonian H up to moment t is given by

$$|\psi(t)\rangle = \frac{e^{-iHt}|\psi_0\rangle}{\|e^{-iHt}|\psi_0\rangle\|}, \tag{A1}$$

which can be further written as

$$\begin{aligned}|\psi(t)\rangle &= \frac{1}{\sqrt{N(t)}} e^{-iHt} \prod_{j=1}^{L/2} c_{2j}^\dagger |\text{vac}\rangle \\ &= \frac{1}{\sqrt{N(t)}} \prod_{j=1}^{L/2} c_{2j}^\dagger(t) |\text{vac}\rangle,\end{aligned} \tag{A2}$$

where $N(t) = \|e^{-iHt}|\psi_0\rangle\|$, and $c_j^\dagger(t) = e^{-iHt} c_j^\dagger e^{iHt}$. We see that the evolved $|\psi(t)\rangle$ remains a determinant, except that the operator $c_{2j}^\dagger(t)$ is not necessarily orthogonal. We can write the unnormalized evolving state as

$$\begin{aligned}\left|\tilde{\psi}(t)\right\rangle &= \prod_{j=1}^{L/2} c_{2j}^\dagger |\text{vac}\rangle \\ &= \left[\prod_{k=1}^{L/2} \left(\sum_{j=1}^{L} [U(t)]_{jk} c_j^\dagger\right)\right] |\text{vac}\rangle,\end{aligned} \tag{A3}$$

where $U(t) = e^{-iHt} U_0$, and U_0 is an $L \times \frac{L}{2}$ matrix representing the set of all initial single-particle states with $[U_0]_{jk} = \delta_{j,2k}$. In this representation, the matrix $U(t)$ contains all information about the quantum dynamics. As the Hamiltonian is non-Hermitian, the elements in $U(t)$ may grow or decay exponentially with t. Therefore, we need to determine smaller step sizes Δt to prevent non-Hermitian instability. After the time interval Δt, the state evolves as

$$\begin{aligned}|\psi(t+\Delta t)\rangle &\propto e^{iH\Delta t}|\psi(t)\rangle \\ &= \left[\prod_{k=1}^{L/2} \left(\sum_{j=1}^{L} [e^{iH\Delta t} U]_{jk}(t) c_j^\dagger\right)\right] |\text{vac}\rangle.\end{aligned} \tag{A4}$$

To restore the normalization condition $\langle\psi|\psi\rangle = 1$, we perform the QR decomposition,

$$U(t) = e^{iHt} U_0 = QR, \tag{A5}$$

where Q is an $L \times \frac{L}{2}$ matrix satisfying $Q^\dagger Q = 1$, and R is an upper triangular matrix. The $L \times \frac{L}{2}$ matrix $U(t+\Delta t)$ is obtained as

$$U(t+\Delta t) = Q. \tag{A6}$$

For our calculations, $\Delta t \leqslant 5$ was chosen to prevent non-Hermitian induced numerical instabilities.

The correlation function $C_{ij}(t) = \langle\psi(t)|c_i^\dagger c_j|\psi(t)\rangle$ in time t, and the von Neumann entanglement entropy S between a subsystem $[x_1, x_2]$ and the rest of the system by [82]

$$S = -\sum_{i=1}^{x_2 - x_1 + 1} [V_i \ln(V_i) + (1 - V_i)\ln(1 - V_i)], \tag{A7}$$

where V_i is the ith eigenvalue of the correlation matrix. In the main text,we have only considered the half chain, i.e., $x_1 = 1$, $x_2 = L/2$. The density of site j at time t is

$$n_j = C_{jj}(t). \tag{A8}$$

APPENDIX B: THE LOCALIZATION PHASE TRANSITION

We can transform the Hamiltonian Eq. (1) with OBCs into the Hermitian AAH Hamiltonian H' by similarity transformation

$$H' = SHS^{-1} = \begin{pmatrix} V_1 & J' & & \\ J' & V_2 & J' & \\ & \ddots & \ddots & J' \\ & & J' & V_L \end{pmatrix}, \tag{B1}$$

where $J' = \sqrt{J_R J_L}$, $V_j = 2\lambda\cos(2\pi\alpha j + \theta)$, the similarity matrix $S = \mathrm{diag}(e^{-g}, e^{-2g}, \ldots, -e^{Lg})$, and $g = \sqrt{J_R/J_L}$. For the Hermitian's AAH model H', $\lambda/J' = 1$ is the localization phase transition point. Let ψ' be the eigenstate of the Hamiltonian H', then for the eigenstate ψ of the Hamiltonian H, it satisfies $\psi = S^{-1}\psi'$. Thus, for an extended eigenstate of the Hamiltonian H', S^{-1} makes the wave function exponential localized on the boundary. For a localized state, the wave function is

$$|\psi_j| \propto \begin{cases} e^{-(\eta+g)(j-j_0)}, & j > j_0, \\ e^{-(\eta-g)(j_0-j)}, & j < j_0, \end{cases} \tag{B2}$$

where j_0 is the index of the localization center and $\eta = \ln(\lambda/J') > 0$ is the Lyapunov exponent for Hamiltonian H'. There are two different Lyapunov exponents $\eta \pm g$ on both sides of the localized center. When $\eta \leqslant |g|$, the system shows the delocalized Anderson mode and the emergence of a skin mode on the same side and the corresponding boundary of the skin/localization phase is given by $\lambda = \max\{J_L, J_R\}$ [41].

Numerically, the transition from the skin phase to the Anderson localized phase can be described by the following physical quantities.

The first is the fractal dimension Γ. We may evaluate the moments $\xi_q(\beta) = \sum_{j=1}^{L} |\psi_j(\beta)|^{2q} \propto L^{-\Gamma_q(q-1)}$ for the βth eigenstate $|\psi(\beta)\rangle = \sum_j \psi_j(\beta)|j\rangle$ [63,65,69,72], where Γ_q represents the fractal dimensions. For the next calculations, we choose $q = 2$ to describe the localization phase transition, while ξ_2 represents the inverse participation ratio. Thus, the fractal dimension at finite size can be written as

$$\Gamma(\beta) = -\frac{\ln \xi(\beta)}{\ln L}, \tag{B3}$$

where we omit the subscripts Γ_2 and ξ_2. For an extended (localized) state, $\Gamma \to 1$ ($\Gamma \to 0$), and $0 < \Gamma < 1$ for a multifractal state. It should be noted that the extended (localized) states become more and more extended (localized) with increasing system size and the fractal dimension Γ in the thermodynamic limit $L = \infty$ becomes equal to 1 (0), while the fractal dimension Γ of the multifractal state in the thermodynamic limit remain between 0 and 1. Thus, by calculating the finite size behavior of the fractal dimension for different system sizes, results in the thermodynamic limit can be obtained by interpolation to account for the localization properties of the eigenstates [73]. Since there are no mobility edges in the non-Hermitian AAH model, we further define the average fractal dimension $\overline{\Gamma} = \frac{1}{L}\sum_{\beta=1}^{L}\Gamma(\beta)$ to account for the localization phase transition.

Second, the skin effect stems from the nontrivial topological properties of the system [28,34,41]. We can define the winding number of the reference point E_b in the complex plane

$$\omega = \int_0^{2\pi} \frac{\partial_\Phi \ln\det[H(\Phi) - E_b]}{2\pi i} d\Phi, \tag{B4}$$

where $H(\Phi) = H + J_R e^{-i\Phi} + J_L e^{i\Phi}$ and Φ is a magnetic flux. When $\omega = 1\,(-1)$, it has a left (right) skin phase under the OBC, while $\omega = 0$ has no skin effect. Moreover, under the skin phase, the Hamiltonian Eq. (1) is particularly sensitive to boundary conditions, and the complex eigenvalues vanish under OBCs. In the localized phase, the eigenvalues are all real independently of the boundary conditions [41]. We can define the eigenvalue maximal imaginary part,

$$\max(\mathrm{Im}E) = \max_{\beta=1,\ldots L}(|\mathrm{Im}E_\beta|), \tag{B5}$$

to describe the skin-Anderson localization phase transition.

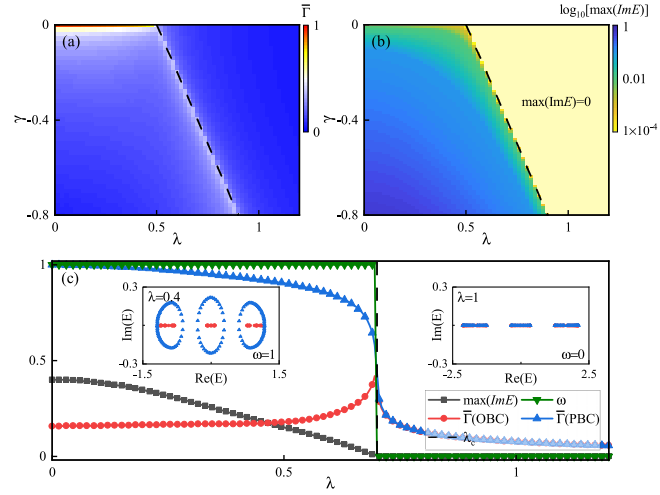

FIG. 5. (a) The average fractal dimension $\overline{\Gamma}$ and (b) $\max(\mathrm{Im}E)$ on the $\lambda - \gamma$ plane, where the black dashed line is $\lambda = (J - \gamma)/2$. (c) The average fractal dimension $\overline{\Gamma}$, $\max(\mathrm{Im}E)$, and winding number ω as a function of λ for $\gamma = -0.4$, where the inset shows the eigenvalues under PBCs (blue triangles) and OBCs (red circles) in the complex plane for system size $L = 144$. For all main plots, we set $L = 610$ and $\theta = 0$.

In Figs. 5(a) and 5(b), we show the average fractal dimension $\overline{\Gamma}$ under OBCs and $\max(\mathrm{Im}E)$ under PBCs, respectively. When $\gamma = 0$, $\lambda = 0.5$ is the phase transition point for the extended and localized regions. When $\gamma < 0$, $\max(\mathrm{Im}E) > 0$ shows that the system has a nontrivial topological point gap, in which case the eigenstates exhibit a skin effect under OBCs, making Γ tend to 0. However, at the critical line $\lambda = (J - \gamma)/2$, the $\overline{\Gamma}$ exhibits a peak, and the eigenvalue under PBC undergoes a complex-realistic transition, and the skin effect disappears. Specifically, in Fig. 5(c), we show $\max(\mathrm{Im}E)$, $\overline{\Gamma}$, and ω as a function of λ for $\gamma = -0.4$. The $\max(\mathrm{Im}E) > 0$ and $\omega = 1$, showing that the system has a nontrivial topological point gap in the region $\lambda < \lambda_c$, causing $\overline{\Gamma} \to 0$ under OBCs due to the skin effect, while $\overline{\Gamma} \to 1$ under PBCs is the extended phase. We can see the case of $\lambda = 0.4$ in the inset in Fig. 5(c), where in the complex plane, the PBC eigenenergy spectrum contains the eigenvalues of the OBC, and the nontrivial winding number allows for a

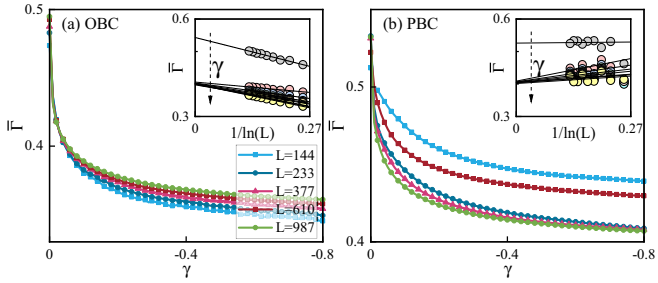

FIG. 6. The average fractal dimension $\overline{\Gamma}$ as a function of γ at the critical line under (a) OBCs and (b) PBCs, where $\lambda = (J-\gamma)/2$. The inset shows the $\overline{\Gamma}$ as a function of $\ln(L)$ for γ from 0 to -0.8 and $\lambda = (J-\gamma)/2$. For all plots, we set $\theta = 0$.

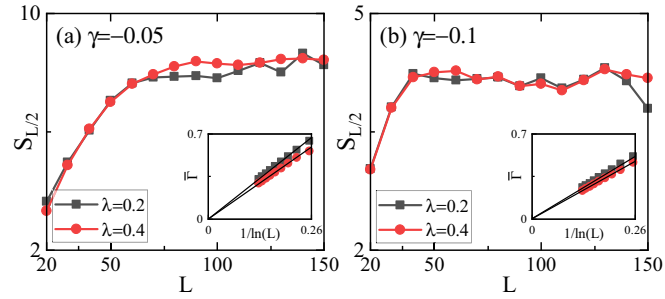

FIG. 7. The entanglement entropy $S_{L/2}$ as a function of L for different λ with (a) $\gamma = -0.05$ and (b) $\gamma = -0.1$. The inset shows the $\overline{\Gamma}$ as a function of $\ln(L)$ for different λ.

skin effect under OBCs. When $\lambda > \lambda_c$, the nontrivial point gap vanishes, $\max(\mathrm{Im}E)$, $\omega = 0$, and the system undergoes Anderson localization (the case of $\lambda = 1$ in the inset). The system undergoes multiple phase transitions on the critical line $\lambda = \lambda_c$, i.e., localization phase transitions, eigenvalue complex-real phase transitions, and topological phase transitions. To understand the volume law that emerges at the critical line, we further discuss the effect of non-Hermitian hopping on the multifractal phase. In Figs. 6(a) and 6(b), we show the average fractal dimension $\overline{\Gamma}$ at the critical point under OBCs and PBCs, respectively. The results show that the increasing strength of non-Hermitian leads to decreasing $\overline{\Gamma}$ at the critical point, and this enhancement of localization is also reflected in a decrease in the steady-state entanglement entropy [see Figs. 3(b) and 4(c)]. In addition, the $\overline{\Gamma}$ rises slightly with increasing system size under OBCs, whereas it exhibits size-independence under PBCs. We have calculated the $\overline{\Gamma}$ under $L = 55, 89, 144, 233, 377, 610, 987, 1597, 2584$ for γ from 0 to -0.8 in the inset and interpolated to the thermodynamic limit $L \to \infty$ by linear fitting. It can be seen that in the thermodynamic limit, both for OBCs and PBCs, $\gamma < 0$ at $\overline{\Gamma} \sim 0.4$, the system remains multifractal at the critical point, making the entanglement entropy behave as a volume law.

APPENDIX C: SCALING BEHAVIOR OF ENTANGLEMENT ENTROPY UNDER SMALL γ

In the main text, in Fig. 1(a), the system has a large value of entanglement entropy as $\gamma \to 0$ compared to $\gamma < -0.3$. This is due to the fact that the smaller strength of the asymmetric hopping makes the skin effect weaker and the entanglement entropy is able to grow to larger values. In Figs. 7(a) and 7(b), we, respectively, present the steady-state entanglement entropy as the system size increases for $\gamma = -0.05$ and -0.1. It can be observed that, at large system sizes, it satisfies the area law. Also, in the inset we give the average fractal dimension $\overline{\Gamma}$ of the corresponding λ at $L = 55, 89, 144, 233, 377, 610, 987, 1597, 2584$. When the system size is small, it has a large $\overline{\Gamma}$, and the system is less localized. As the size increases and is fitted to the thermodynamic limit, $\overline{\Gamma} = 0$ indicates that it is a localized phase and the entanglement entropy still follows the area law.

[1] R. Blatt and C. F. Roos, Quantum simulations with trapped ions, Nat. Phys. **8**, 277 (2012).

[2] C. Schneider, D. Porras, and T. Schaetz, Experimental quantum simulations of many-body physics with trapped ions, Rep. Prog. Phys. **75**, 024401 (2012).

[3] I. M. Georgescu, S. Ashhab, and F. Nori, Quantum simulation, Rev. Mod. Phys. **86**, 153 (2014).

[4] J. Eisert, M. Friesdorf, and C. Gogolin, Quantum many body systems out of equilibrium, Nat. Phys. **11**, 124 (2015).

[5] T. Langen, R. Geiger, and J. Schmiedmayer, Ultracold atoms out of equilibrium, Annu. Rev. Condens. Matter Phys. **6**, 201 (2015).

[6] C. Gross and I. Bloch, Quantum simulations with ultracold atoms in optical lattices, Science **357**, 995 (2017).

[7] V. V. Konotop, J. Yang, and D. A. Zezyulin, Nonlinear waves in $\mathcal{PT}$-symmetric systems, Rev. Mod. Phys. **88**, 035002 (2016).

[8] R. El-Ganainy, K. G. Makris, M. Khajavikhan, Z. H. Musslimani, S. Rotter, and D. N. Christodoulides, Non-Hermitian physics and PT symmetry, Nat. Phys. **14**, 11 (2018).

[9] Y. Ashida, Z. Gong, and M. Ueda, Non-Hermitian physics, Adv. Phys. **69**, 249 (2020).

[10] C. M. Bender and S. Boettcher, Real spectra in non-Hermitian hamiltonians having $\mathcal{PT}$ symmetry, Phys. Rev. Lett. **80**, 5243 (1998).

[11] A. Guo, G. J. Salamo, D. Duchesne, R. Morandotti, M. Volatier-Ravat, V. Aimez, G. A. Siviloglou, and D. N. Christodoulides, Observation of $\mathcal{PT}$-symmetry breaking in complex optical potentials, Phys. Rev. Lett. **103**, 093902 (2009).

[12] A. Regensburger, C. Bersch, M.-A. Miri, G. Onishchukov, D. N. Christodoulides, and U. Peschel, Parity-time synthetic photonic lattices, Nature (London) **488**, 167 (2012).

[13] S. Weimann, M. Kremer, Y. Plotnik, Y. Lumer, S. Nolte, K. G. Makris, M. Segev, M. C. Rechtsman, and A. Szameit, Topologically protected bound states in photonic parity-time-symmetric crystals, Nat. Mater. **16**, 433 (2017).

[14] X. Ni, D. Smirnova, A. Poddubny, D. Leykam, Y. Chong, and A. B. Khanikaev, $\mathcal{PT}$ phase transitions of edge states at $\mathcal{PT}$ symmetric interfaces in non-Hermitian topological insulators, Phys. Rev. B **98**, 165129 (2018).

[15] M. Kremer, T. Biesenthal, L. J. Maczewsky, M. Heinrich, R. Thomale, and A. Szameit, Demonstration of a two-dimensional $\mathcal{PT}$-symmetric crystal, Nat. Commun. **10**, 435 (2019).
[16] S. Xia, D. Kaltsas, D. Song, I. Komis, J. Xu, A. Szameit, H. Buljan, K. G. Makris, and Z. Chen, Nonlinear tuning of PT symmetry and non-Hermitian topological states, Science **372**, 72 (2021).
[17] Y. Li, C. Liang, C. Wang, C. Lu, and Y.-C. Liu, Gain-loss induced hybrid skin-topological effect, Phys. Rev. Lett. **128**, 223903 (2022).
[18] P. Peng, W. Cao, C. Shen, W. Qu, J. Wen, L. Jiang, and Y. Xiao, Anti-parity-time symmetry with flying atoms, Nat. Phys. **12**, 1139 (2016).
[19] J. Li, A. K. Harter, J. Liu, L. de Melo, Y. N. Joglekar, and L. Luo, Observation of parity-time symmetry breaking transitions in a dissipative Floquet system of ultracold atoms, Nat. Commun. **10**, 855 (2019).
[20] Z. Ren, D. Liu, E. Zhao, C. He, K. K. Pak, J. Li, and G.-B. Jo, Chiral control of quantum states in non-Hermitian spin-orbit-coupled fermions, Nat. Phys. **18**, 385 (2022).
[21] L. Xiao, X. Zhan, Z. H. Bian, K. K. Wang, X. Zhang, X. P. Wang, J. Li, K. Mochizuki, D. Kim, N. Kawakami, W. Yi, H. Obuse, B. C. Sanders, and P. Xue, Observation of topological edge states in parity-time-symmetric quantum walks, Nat. Phys. **13**, 1117 (2017).
[22] H.-Z. Li, X.-J. Yu, and J.-X. Zhong, Non-Hermitian stark many-body localization, Phys. Rev. A **108**, 043301 (2023).
[23] X.-J. Yu, Z. Pan, L. Xu, and Z.-X. Li, Non-Hermitian strongly interacting Dirac fermions: A quantum Monte-Carlo study, arXiv:2302.10115.
[24] Z.-X. Guo, X.-J. Yu, X.-D. Hu, and Z. Li, Emergent phase transitions in a cluster Ising model with dissipation, Phys. Rev. A **105**, 053311 (2022).
[25] L. Zhou and D. Zhang, Non-Hermitian floquet topological matter—A review, Entropy **25**, 1401 (2023).
[26] S. Yao and Z. Wang, Edge states and topological invariants of non-Hermitian systems, Phys. Rev. Lett. **121**, 086803 (2018).
[27] Y. Xiong, Why does bulk boundary correspondence fail in some non-Hermitian topological models? J. Phys. Commun. **2**, 035043 (2018).
[28] Z. Gong, Y. Ashida, K. Kawabata, K. Takasan, S. Higashikawa, and M. Ueda, Topological phases of non-Hermitian systems, Phys. Rev. X **8**, 031079 (2018).
[29] K. Kawabata, K. Shiozaki, M. Ueda, and M. Sato, Symmetry and topology in non-Hermitian physics, Phys. Rev. X **9**, 041015 (2019).
[30] C. H. Lee and R. Thomale, Anatomy of skin modes and topology in non-Hermitian systems, Phys. Rev. B **99**, 201103(R) (2019).
[31] K. Yokomizo and S. Murakami, Non-Bloch band theory of non-Hermitian systems, Phys. Rev. Lett. **123**, 066404 (2019).
[32] L. Xiao, T. Deng, K. Wang, G. Zhu, Z. Wang, W. Yi, and P. Xue, Non-Hermitian bulk-boundary correspondence in quantum dynamics, Nat. Phys. **16**, 761 (2020).
[33] K. Zhang, Z. Yang, and C. Fang, Correspondence between winding numbers and skin modes in non-Hermitian systems, Phys. Rev. Lett. **125**, 126402 (2020).
[34] N. Okuma, K. Kawabata, K. Shiozaki, and M. Sato, Topological origin of non-Hermitian skin effects, Phys. Rev. Lett. **124**, 086801 (2020).
[35] D. S. Borgnia, A. J. Kruchkov, and R.-J. Slager, Non-Hermitian boundary modes and topology, Phys. Rev. Lett. **124**, 056802 (2020).
[36] Z. Yang, K. Zhang, C. Fang, and J. Hu, Non-Hermitian bulk boundary correspondence and auxiliary generalized brillouin zone theory, Phys. Rev. Lett. **125**, 226402 (2020).
[37] C.-X. Guo, C.-H. Liu, X.-M. Zhao, Y. Liu, and S. Chen, Exact solution of non-Hermitian systems with generalized boundary conditions: Size-dependent boundary effect and fragility of the skin effect, Phys. Rev. Lett. **127**, 116801 (2021).
[38] L. Li, C. H. Lee, S. Mu, and J. Gong, Critical non-Hermitian skin effect, Nat. Commun. **11**, 5491 (2020).
[39] E. J. Bergholtz, J. C. Budich, and F. K. Kunst, Exceptional topology of non-Hermitian systems, Rev. Mod. Phys. **93**, 015005 (2021).
[40] K. Kawabata, T. Numasawa, and S. Ryu, Entanglement phase transition induced by the non-Hermitian skin effect, Phys. Rev. X **13**, 021007 (2023).
[41] H. Jiang, L.-J. Lang, C. Yang, S.-L. Zhu, and S. Chen, Interplay of non-Hermitian skin effects and Anderson localization in nonreciprocal quasiperiodic lattices, Phys. Rev. B **100**, 054301 (2019).
[42] K. Li, Z.-C. Liu, and Y. Xu, Disorder-induced entanglement phase transitions in non-Hermitian systems with skin effects, arXiv:2305.12342.
[43] R. Hamazaki, K. Kawabata, and M. Ueda, Non-Hermitian many-body localization, Phys. Rev. Lett. **123**, 090603 (2019).
[44] T. Orito and K.-I. Imura, Entanglement dynamics in the many-body Hatano-Nelson model, Phys. Rev. B **108**, 214308 (2023).
[45] X. Turkeshi and M. Schiró, Entanglement and correlation spreading in non-Hermitian spin chains, Phys. Rev. B **107**, L020403 (2023).
[46] Y. Le Gal, X. Turkeshi, and M. Schiro, Volume-to-area law entanglement transition in a non-Hermitian free fermionic chain, SciPost Phys. **14**, 138 (2023).
[47] X. Zhang, T. Zhang, M.-H. Lu, and Y.-F. Chen, A review on non-Hermitian skin effect, Adv. Phys. **7**, 2109431 (2022).
[48] D.-W. Zhang, L.-Z. Tang, L.-J. Lang, H. Yan, and S.-L. Zhu, Non-Hermitian topological Anderson insulators, Sci. China Phys. Mech. Astron. **63**, 267062 (2020).
[49] D.-W. Zhang, Y.-L. Chen, G.-Q. Zhang, L.-J. Lang, Z. Li, and S.-L. Zhu, Skin superfluid, topological mott insulators, and asymmetric dynamics in an interacting non-Hermitian Aubry-André-Harper model, Phys. Rev. B **101**, 235150 (2020).
[50] L.-J. Lang, S.-L. Zhu, and Y. D. Chong, Non-Hermitian topological end breathers, Phys. Rev. B **104**, L020303 (2021).
[51] Z. Gong, S. Higashikawa, and M. Ueda, Zeno Hall effect, Phys. Rev. Lett. **118**, 200401 (2017).
[52] J. Eisert, M. Cramer, and M. B. Plenio, *Colloquium*: Area laws for the entanglement entropy, Rev. Mod. Phys. **82**, 277 (2010).
[53] R. Nandkishore and D. A. Huse, Many-body localization and thermalization in quantum statistical mechanics, Annu. Rev. Condens. Matter Phys. **6**, 15 (2015).
[54] N. Roy and S. Auditya, Entanglement entropy and out-of-time-order correlator in the long-range Aubry-André-Harper model, J. Phys.: Condens. Matter **33**, 334001 (2021).
[55] P. W. Anderson, Absence of diffusion in certain random lattices, Phys. Rev. **109**, 1492 (1958).

[56] S. Aubry and G. André, Analyticity breaking and Anderson localization in incommensurate lattices, Ann. Israel Phys. Soc **3**, 133 (1980).
[57] F. Evers and A. D. Mirlin, Anderson transitions, Rev. Mod. Phys. **80**, 1355 (2008).
[58] A. Lagendijk, B. van Tiggelen, and D. S. Wiersma, Fifty years of Anderson localization, Phys. Today **62**, 24 (2009).
[59] E. Abrahams, *50 Years of Anderson Localization* (World Scientific Publishing, Singapore, 2010).
[60] E. Abrahams, P. W. Anderson, D. C. Licciardello, and T. V. Ramakrishnan, Scaling theory of localization: Absence of quantum diffusion in two dimensions, Phys. Rev. Lett. **42**, 673 (1979).
[61] S.-Z. Li, X.-J. Yu, S.-L. Zhu, and Z. Li, Anderson localization and swing mobility edge in curved spacetime, Phys. Rev. B **108**, 094209 (2023).
[62] S. Lellouch and L. Sanchez-Palencia, Localization transition in weakly-interacting Bose superfluids in one-dimensional quasiperdiodic lattices, Phys. Rev. A **90**, 061602(R) (2014).
[63] H. Yao, H. Khouldi, L. Bresque, and L. Sanchez-Palencia, Critical behavior and fractality in shallow one-dimensional quasi-periodic potentials, Phys. Rev. Lett. **123**, 070405 (2019).
[64] T. Liu, X. Xia, S. Longhi, and L. Sanchez-Palencia, Anomalous mobility edges in one-dimensional quasiperiodic models, SciPost Phys. **12**, 027 (2022).
[65] X. Deng, S. Ray, S. Sinha, G. V. Shlyapnikov, and L. Santos, One-dimensional quasicrystals with power-law hopping, Phys. Rev. Lett. **123**, 025301 (2019).
[66] N. Roy and A. Sharma, Fraction of delocalized eigenstates in the long-range Aubry-André-Harper model, Phys. Rev. B **103**, 075124 (2021).
[67] J. Biddle and S. Das Sarma, Predicted mobility edges in one-dimensional incommensurate optical lattices: an exactly solvable model of anderson localization, Phys. Rev. Lett. **104**, 070601 (2010).
[68] S. Ganeshan, J. H. Pixley, and S. Das Sarma, Nearest neighbor tight binding models with an exact mobility edge in one dimension, Phys. Rev. Lett. **114**, 146601 (2015).
[69] Y. Wang, X. Xia, L. Zhang, H. Yao, S. Chen, J. You, Q. Zhou, and X.-J. Liu, One-dimensional quasiperiodic mosaic lattice with exact mobility edges, Phys. Rev. Lett. **125**, 196604 (2020).
[70] S.-Z. Li and Z. Li, The multiple re-entrant localization in a phase-shift quasiperiodic chain, arXiv:2305.12321.
[71] A. Padhan, M. Giri, S. Mondal, and T. Mishra, Emergence of multiple localization transitions in a one-dimensional quasiperiodic lattice, Phys. Rev. B **105**, L220201 (2022).
[72] D. D. Vu and S. Das Sarma, Generic mobility edges in several classes of duality-breaking one-dimensional quasiperiodic potentials, Phys. Rev. B **107**, 224206 (2023).
[73] Y. Wang, L. Zhang, W. Sun, T. F. J. Poon, and X.-J. Liu, Quantum phase with coexisting localized, extended, and critical zones, Phys. Rev. B **106**, L140203 (2022).
[74] P. G. Harper, Single band motion of conduction electrons in a uniform magnetic field, Proc. Phys. Soc. A **68**, 874 (1955).
[75] L.-J. Zhai, S. Yin, and G.-Y. Huang, Many-body localization in a non-Hermitian quasiperiodic system, Phys. Rev. B **102**, 064206 (2020).
[76] S. Longhi, Phase transitions in a non-Hermitian Aubry-André-Harper model, Phys. Rev. B **103**, 054203 (2021).
[77] A. Chakrabarty and S. Datta, Skin effect and dynamical delocalization in non-Hermitian quasicrystals with spin-orbit interaction, Phys. Rev. B **107**, 064305 (2023).
[78] Y.-C. Wang, K. Suthar, H. H. Jen, Y.-T. Hsu, and J.-S. You, Non-Hermitian skin effects on thermal and many-body localized phases, Phys. Rev. B **107**, L220205 (2023).
[79] L.-J. Zhai, G.-Y. Huang, and S. Yin, Nonequilibrium dynamics of the localization-delocalization transition in the non-Hermitian Aubry-André model, Phys. Rev. B **106**, 014204 (2022).
[80] T. Orito and K.-I. Imura, Unusual wave-packet spreading and entanglement dynamics in non-Hermitian disordered many-body systems, Phys. Rev. B **105**, 024303 (2022).
[81] N. Hatano and D. R. Nelson, Localization transitions in non-Hermitian quantum mechanics, Phys. Rev. Lett. **77**, 570 (1996).
[82] I. Peschel, Calculation of reduced density matrices from correlation functions, J. Phys. A **36**, L205 (2003).
[83] A. Panda and S. Banerjee, Entanglement in nonequilibrium steady states and many-body localization breakdown in a current-driven system, Phys. Rev. B **101**, 184201 (2020).
[84] L. Zhou, companion paper, Entanglement phase transitions in non-Hermitian quasicrystals, Phys. Rev. B **109**, 024204 (2024).